Sensors & Actuators: B. Chemical 427 (2025) 137136

Contents lists available at ScienceDirect

Sensors and Actuators: B. Chemical

journal homepage: www.elsevier.com/locate/snb

Electrochemiluminescence resonance energy transfer biosensor based on BNCs@Zn-PTC for ultrasensitive and low-potential detection of CA125 in pancreatic cancer diagnostics

Yuxuan Chen [a], Zhuoxin Ye [a], Mo Ma [a,b], Yongli Wu [a], Jukun Yang [a], Pinyi Ma [a,*], Ziwei Zhang [a,*], Daqian Song [a]

[a] *College of Chemistry, Jilin Province Research Center for Engineering and Technology of Spectral Analytical Instruments, Jilin University, Qianjin Street 2699, Changchun 130012, China*
[b] *School of Pharmacy, Jilin University, Qianjin Street 2699, Changchun 130012, China*

ARTICLE INFO

Keywords:
Electrochemiluminescence
CA125
ECL-RET
Biosensor
Pancreatic adenocarcinoma

ABSTRACT

At present, surgical resection is the primary clinical treatment method for pancreatic cancer. Accurate assessment of resectability is crucial for effective treatment planning. This paper focuses on the detection of carbohydrate antigen 125 (CA125), the *in vitro* biomarker for determining the resectability of pancreatic cancer. We prepared a highly stable electrochemiluminescence (ECL) luminophore, Zn-PTC, by coordinating perylene tetracarboxylic acid (PTCA) with Zn^{2+} ions. However, the current applications of Zn-PTC as ECL luminophores face challenges due to their high luminescence potential. To address these challenges, we introduced the ECL resonance energy transfer (ECL-RET) strategy and synthesized a composite material, BNCs@Zn-PTC, to achieve low-potential anodic ECL luminescence. In the ECL-RET system, Zn-PTC serves as the energy donor, while gold-silver bimetallic nanoclusters (Au-Ag BNCs) act as the energy acceptor. UV-Vis spectra of Au-Ag BNCs partially overlapped with the ECL spectra of Zn-PTC, which facilitate to effective ECL-RET between the donor and the acceptor. Utilizing BNCs@Zn-PTC as ECL luminophores, we constructed a strand displacement reaction-catalyzed hairpin assembly (SDR-CHA) dual *in vitro* amplified ECL sensor to detect the target CA125. Under optimal experimental conditions, the sensor had a linear detection range at CA125 concentration from 1 μU mL^{-1} to 10 U mL^{-1}, with a detection limit of 0.24 μU mL^{-1}. This study presents a novel approach for developing low-potential ECL-emitting luminophores with significant potential in clinical applications.

1. Introduction

Pancreatic cancer (PC) is one of the most malignant gastrointestinal tumors with a 5-year survival rate of approximately 12 % [1,2]. Surgical resection remains the primary treatment [3]. Early diagnosis can significantly improve survival rates, and accurate prognosis prediction is essential for surgical decision-making and postoperative outcome forecasting [4,5]. Currently, imaging is the main tool for early diagnosis and postoperative prediction; nonetheless, it is time-consuming, costly, and often lacks accuracy [6]. Therefore, identifying a suitable molecular biomarker for blood testing could significantly enhance diagnostic efficiency. Both carbohydrate antigen 125 (CA125) and carbohydrate antigen 19-9 (CA19-9) have high specificity and sensitivity to pancreatic cancer and thus are essential to the clinical diagnosis of this type of cancer [7,8]. Notably, in predicting resectability, CA125 is highly sensitive, with a critical threshold between 34 and 35 U mL^{-1} [9]. Consequently, the ability to specifically detect CA125 in blood can be of great clinical significance for pancreatic cancer management.

Electrochemiluminescence (ECL) is increasingly used in critical areas, such as disease marker detection, due to its low cost, controllability, and high sensitivity [10–12]. Luminophores are an integral part of the ECL system. Perylene, a common polycyclic aromatic hydrocarbon (PAH), offers many advantages such as excellent photostability, high ECL intensity, and ease of synthesis [13–15]. Existing studies on perylene in ECL sensing mainly focus on cathodoluminescence [16–18]. A few studies have highlighted a significant drawback of anodoluminescence, which is the high luminescence potential that has limited its application in ECL sensing [19]. In recent years, MOF nanosheets, as an

---

* Corresponding authors.
E-mail addresses: mapinyi@jlu.edu.cn (P. Ma), zzw@jlu.edu.cn (Z. Zhang).

https://doi.org/10.1016/j.snb.2024.137136
Received 16 October 2024; Received in revised form 2 December 2024; Accepted 14 December 2024
Available online 16 December 2024

emerging new type of 2D materials, have attracted considerable attention due to their ultra-thinness and relatively large specific surface area [20,21]. Combining perylene and metal ions to construct novel MOF nanosheets can be a promising strategy for improving the luminescence performance of perylene [22–24]. However, the electrical conductivity of MOFs largely limits their ECL sensing performance. Thus, integrating MOFs with noble metal nanoclusters can effectively improve the conductivity of ECL luminophores [25,26]. Nevertheless, single-metal nanoclusters suffer from low ECL emission signals and poor stability in solution [27]. Previous studies have shown that bimetallic nanoclusters (BNCs) can address the weak ECL signal through the synergistic effects among multiple atoms. Using proteins as protecting agents for nanoclusters can enhance stability [28].

Based on these insights, we aimed to combine various materials to leverage their complementary advantages and construct a novel ECL luminophore, BNCs@Zn-PTC. The aggregation-caused quenching (ACQ) effect induced by π-π stacking can be eliminated by coordinating the ligand with Zn^{2+} in Zn-PTC to form MOF nanosheets with a high specific surface area and stable ECL intensity [24]. However, Zn-PTC has high luminescence potential at the anode. To address this problem, we synthesized Au-Ag BNCs that could emit light at the low anodic potential [29]. Then, ECL energy resonance transfer (ECL-RET) is a non-radiative energy transfer process that occurs between a donor and an acceptor, with the exception that it requires the overlap of the donor's ECL spectrum with the acceptor's absorption spectrum [30]. The UV-Vis absorption spectrum of Au-Ag BNCs overlapped well with the ECL spectrum of Zn-PTC, which allows for the establishment of an ECL-RET system that can effectively lower the anodic luminescence potential of the BNCs@Zn-PTC [24,29]. Specifically, BNCs@Zn-PTC were used as ECL luminophores to construct ECL biosensors. In the presence of the co-reactant TEA, BNCs@Zn-PTC exhibited strong ECL intensity at narrow potentials (0–0.9 V). As shown in Scheme 1, Zn-PTC acts as a donor and Au-Ag BNCs as an acceptor, and low potential luminescence at the anode is achieved by modulating the loading ratio. This setup triggers the SDR-CHA double cycling amplification in the presence of the target CA125, thereby significantly quenching the ECL intensity. This ECL biosensor had excellent sensitivity and specificity for CA125 detection. It could effectively differentiate between human normal pancreatic

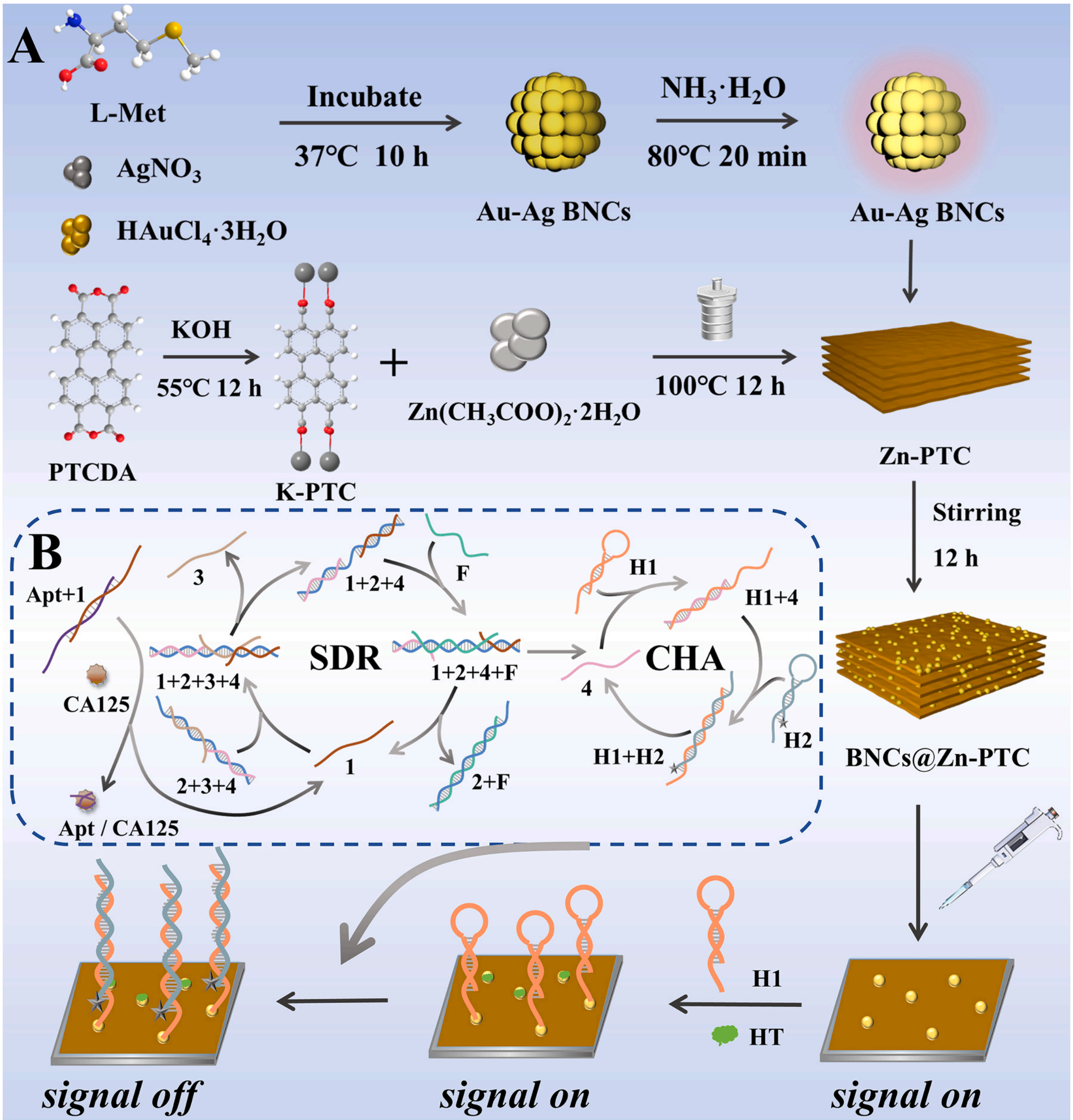

Scheme 1. (A) Preparation of luminophores and assembly of the ECL biosensor. (B) SDR-CHA dual signal amplification process.

(hTERT-HPNE) and pancreatic cancer (PANC-1) cells. It offers a novel approach to pancreatic cancer detection and resectability prediction.

2. Experimental section

2.1. *Synthesis of BNCs@Zn-PTC*

The synthesis procedures for Zn-PTC and Au-Ag BNCs are detailed in the Supporting Information. Briefly, 1.5 mL of Zn-PTC (1.0 mg mL^{-1}) was added dropwise to 3.0 mL of Au-Ag BNCs (1.0 mg mL^{-1}), while stirring. The mixture was stirred overnight at room temperature and was protected from light. The resulting product was collected by centrifugation, dissolved in 3 mL of ultrapure water, and stored away from light at 4 °C.

2.2. *Preparation of reaction solution*

All oligonucleotides (Apt, DNA 1, DNA 2, DNA 3, F, MT, H1 and H2) were dissolved in Tris-HCl buffer to prepare stock solutions. DNA 1 and Apt strands at equal volumes and concentrations were annealed at 95 °C and then slowly cooled to room temperature to allow for the formation of the DNA 1/Apt double-stranded complex. Similarly, a three-stranded complex was formed by annealing DNA 2, DNA 3, and MT at equal volumes and concentrations at 95 °C and cooling to room temperature. Hairpin strands H1 and H2 were annealed at 95 °C and cooled to 25 °C. The annealed H1 strand was treated with TCEP at 37 °C for 40 min to reduce disulfide bonds.

Different concentrations of CA125 were mixed with the DNA 1/Apt double-stranded complex (2 μM) and reacted at 37 °C for 40 min to obtain the target reaction solution. The target reaction solution was then mixed with the triple-stranded complex (2 μM) and F strand (2 μM) and reacted at 37 °C for 85 min to complete the preparation of the reaction solution.

2.3. *Construction of the ECL biosensor*

Prior to electrode modification, a glassy carbon electrode (GCE) was polished with 0.3 μM and 0.5 μM alumina powder, followed by sonication in ethanol and ultrapure water to remove residual alumina powder. This step yielded a clean electrode interface. The treated GCE was air-dried, drop-casted with 10 μL of BNCs@Zn-PTC (0.16 mg mL^{-1}) on its surface, and then dried at 37 °C. Subsequently, 10 μL of H1 chain (1.5 μM) was drop-casted on the surface of the modified electrode and incubated overnight at room temperature. The electrode was then washed with PBS buffer to remove unbound DNA strands, and 10 μL of HT (1 μM) was drop-casted on the electrode surface and incubated at 37 °C for 40 min to block non-specific binding. After the reaction was complete, the electrode was washed with deionized water. Finally, 10 μL of H2 chain (2 μM) and the reaction solution were drop-casted on the electrode surface and incubated at 37 °C for 105 min to complete the assembly of the sensor electrode.

2.4. *Measurement conditions*

For this research, the test solution comprised 20 mM TEA in 0.1 M PBS (pH = 7.4). The measurement parameters were set as follows: potential range, 0–0.9 V; photomultiplier tube high voltage, 800 V; and scanning speed, 0.5 V/s.

3. Results and discussion

3.1. *Characterization of materials*

The morphology of Zn-PTC was first characterized by scanning electron microscopy (SEM). As depicted in Fig. 1A, Zn-PTC exhibited a lamellar structure with a particle size of approximately 200 nm [31]. Further analysis was conducted using Fourier-transform infrared spectroscopy (FT-IR). Compared to the 3,4,9,10-tetracarboxylic acid dihydride (PTCDA) precursor, the FT-IR spectra of Zn-PTC (Fig. S1) showed the disappearance of characteristic peaks corresponding to the C═O stretching vibrations (1772, 1756, 1742, and 1730 cm^{-1}) and C-O-C stretching vibrations (1301 and 1235 cm^{-1}). Additionally, the COO^{-} stretching vibrations (1545 and 1360 cm^{-1}) were observed, which is an indication of the coordination between the carboxylic acid group of PTC and Zn^{2+} [22,32]. The composition of Zn-PTC was further analyzed by X-ray photoelectron spectroscopy (XPS) and X-ray diffraction (XRD). The XRD spectrum of Zn-PTC (Fig. S2) revealed several major diffraction peaks that align with previous reports, confirming that the material is crystalline [23]. The XPS spectrum (Fig. S3) showed two significant C 1 s peaks corresponding to the carbon of the cyclic vinyl ring and ester carbon-based carbon (O═C-O) at 285.1 and 288.9 eV, respectively. The O 1 s spectrum displayed binding energies at 532.3 and 533.6 eV, which can be assigned to ester carbon-based oxygen (O═C-O) and oxygen in crystal water, respectively [22]. Elemental mapping analysis (Fig. 1B) further confirmed the presence of Zn, O, and C in Zn-PTC, corroborating the results obtained from the XPS and XRD analyses. These

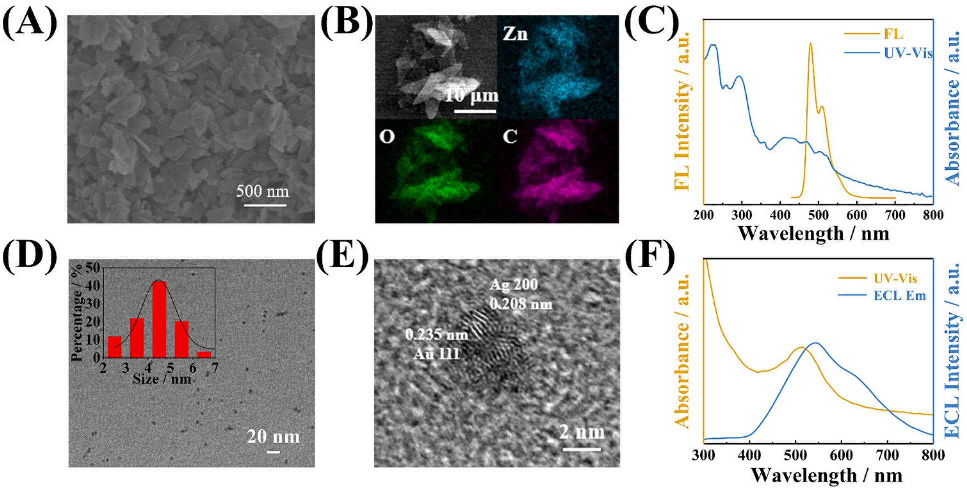

Fig. 1. (A) SEM morphology of Zn-PTC. (B) Element mapping image of Zn-PTC. (C) Fluorescence spectra (blue line) and UV-Vis absorption spectra (yellow line) of Zn-PTC. (D) TEM morphology of Au-Ag BNCs. (E) Enlarged views of the HRTEM image of Au−Ag BNCs. (F) ECL spectra of Zn-PTC (blue line) and UV absorption spectra of Au-Ag BNCs (yellow line). Inset of D shows the particle size of Au-Ag BNCs.

comprehensive results demonstrate the successful synthesis of high-purity Zn-PTC. The optical properties of Zn-PTC were characterized by UV-Vis spectroscopy, fluorescence (FL) spectroscopy, and ECL spectroscopy. The maximum FL emission peak of Zn-PTC was observed at 490 nm (excitation wavelength = 430 nm). The characteristic UV-Vis peaks at 304 nm and 500 nm confirmed the coordination of Zn^{2+} (Fig. 1C). The ECL emission of Zn-PTC (Fig. 1F) was red-shifted by 50 nm compared to the PL emission, which could be attributed to the self-absorption of Zn-PTC or instrumental effects during ECL spectroscopic measurement.

The morphology of Au-Ag BNCs was characterized by transmission electron microscopy (TEM). As shown in Fig. 1D, the average particle size of Au-Ag BNCs was approximately 5 nm [29]. The high-resolution TEM (HRTEM) pattern (Fig. 1E) displayed lattice fringes of 0.235 nm and 0.208 nm, corresponding to the 111 crystallographic plane of Au and the 200 crystallographic plane of Ag, respectively. These findings were corroborated by the XRD results (Fig. S2). The XPS spectra provided information on the elemental composition and valence states of the material surface. As shown in Fig. S4, Au, Ag, and S elements were presented in Au-Ag BNCs. The Ag 3d binding energy peaks were located at 367.9 eV and 373.9 eV, which are consistent with zero-valence Ag, an indication that monovalent Ag was reduced by the ligand and incorporated into the bimetallic nanoclusters. The Au 4 f peaks at 84.1 eV and 87.8 eV indicated the simultaneous presence of zero-valent and monovalent Au. The FT-IR spectrum (Fig. S1) showed that the -C-S stretching vibration in the region of 790–830 cm^{-1} was suppressed, and the characteristic peaks of $-NH_2$ (1615 cm^{-1}) and -COOH (1533 cm^{-1}) remained almost unchanged. Additionally, the UV-Vis absorption peak of Au-Ag BNCs was observed at around 530 nm (Fig. 1F), which is consistent with previous reports [29]. These comprehensive results demonstrate the successful synthesis of Zn-PTC and Au-Ag BNCs.

The HRTEM images (Fig. 2B) and elemental mapping analysis results (Fig. 2A) confirmed the successful loading of Au-Ag BNCs onto lamellar Zn-PTC. The XRD spectra (Fig. S2) revealed that compared with Zn-PTC alone, BNCs@Zn-PTC exhibited additional characteristic peaks of BNCs. The XPS results (Fig. 2C and Fig. S5) further demonstrated the presence of elements from both Zn-PTC and Au-Ag BNCs in the composite material. Fig. 2D presents the thermogravimetric analysis (TGA) curves of Zn-PTC and BNCs@Zn-PTC. The TGA curve of Zn-PTC aligned with previous related reports [22], while the curve of BNCs@Zn-PTC showed that there was a slight increase in weight loss after the addition of Au-Ag BNCs. This may be attributed to the fact that the weight loss of Au-Ag BNCs is less significant than that of Zn-PTC. The overlap of the curves in the initial stages is due to the similar weight loss temperature of Au-Ag BNCs and Zn-PTC, which is about 350 °C [33].

These findings collectively verify that Au-Ag BNCs were successfully integrated into the Zn-PTC structure to form the composite material BNCs@Zn-PTC.

3.2. ECL performance of BNCs@Zn-PTC

To determine the optimal ECL performance of BNCs@Zn-PTC, we optimized the synthesis conditions of the composites. As shown in Fig. 3A, the ECL intensity increased as the Au-Ag BNCs:Zn-PTC ratio varied from 1:0.1 to 1:0.5 and reached its peak at 1:0.5. Based on these findings, the optimal reaction time was identified. Fig. 3B demonstrates that the ECL intensity significantly increased with increasing reaction time, reaching its peak value at 8 h. Thus, 8 h was chosen as the optimal reaction time.

To investigate the factors affecting the ECL intensity of BNCs@Zn-PTC, we examined the luminescence mechanism of Au-Ag BNCs in the presence of TEA as a co-reactant. As shown in Fig. 3C, compared to bare GCE (curve a), Au-Ag BNCs exhibited two oxidation processes in 0.1 M PBS, occurring at 0.87 V and 1.44 V, respectively (curve c). Additionally, the oxidation process of TEA was observed in 0.1 M PBS, with the maximum oxidation peak near 1.12 V (curve b). However, for Au-Ag BNCs in the presence of TEA as a co-reactant (curve d), the oxidation peak at 0.87 V was significantly enhanced. In the Au-Ag BNCs/TEA binary ECL system, Au-Ag BNCs were first oxidized to Au-Ag $BNCs^{\bullet+}$, followed by the oxidation of TEA to $TEA^{\bullet+}$. The radical $TEA^{\bullet+}$ generated during this process can inject electrons into nanoparticles or nanoparticles in the hole-injected state, leading to oxidized-reduced ECL radiation through electron and hole annihilation reactions.

BNCs@Zn-PTC was synthesized under the above conditions, and its ECL luminescence intensity and potential were compared with those of Zn-PTC and Au-Ag BNCs. As shown in Fig. 3D, Zn-PTC exhibited an ECL intensity of 17366 a.u. at 1.3 V, whereas the composite BNCs@Zn-PTC exhibited an ECL intensity of 16203 a.u. at 0.87 V. Under the same conditions, pure Au-Ag BNCs exhibited an ECL intensity of 3889 a.u. This indicates that under the influence of Zn-PTC, the ECL intensity of Au-Ag BNCs increased by 3.2 times. Moreover, the ECL efficiency of the composite BNCs@Zn-PTC was 5.67 times higher than that of Au-Ag BNCs alone (Supporting Information S2.9).

A comparison of cyclic voltammetry (CV) curves in Fig. 3E shows that the strongest oxidation peak of Zn-PTC appeared near 1.12 V (curve b). In contrast, the oxidation peak of the composite BNCs@Zn-PTC

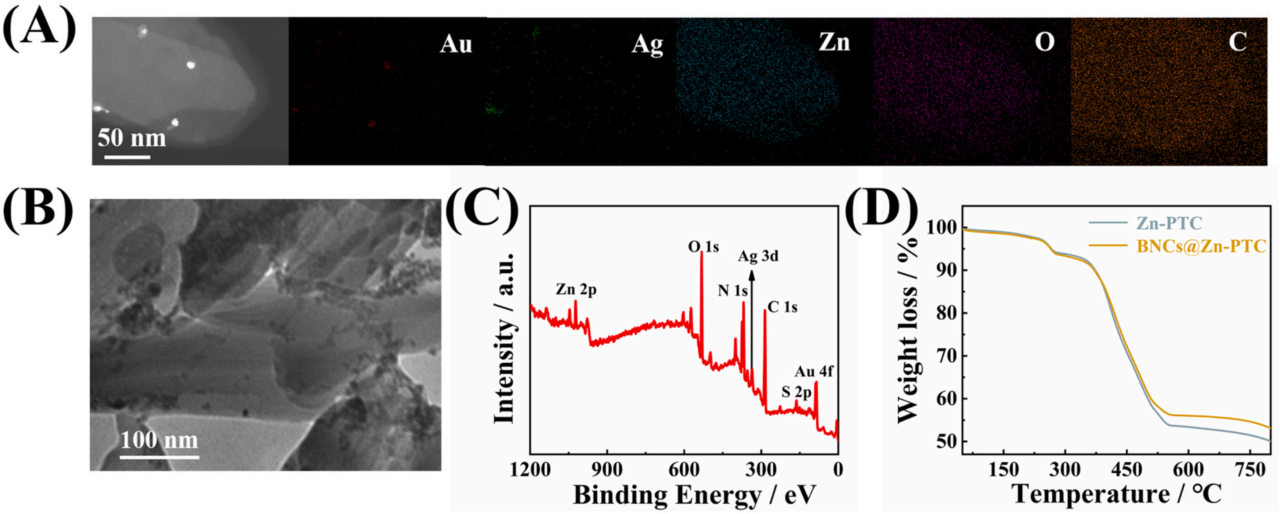

Fig. 2. (A) Element mapping image of BNCs@Zn-PTC. (B) TEM morphology of BNCs@Zn-PTC. (C) XPS scans for the full region of BNCs@Zn-PTC. (D) The TGA curve of Zn-PTC and BNCs@Zn-PTC.

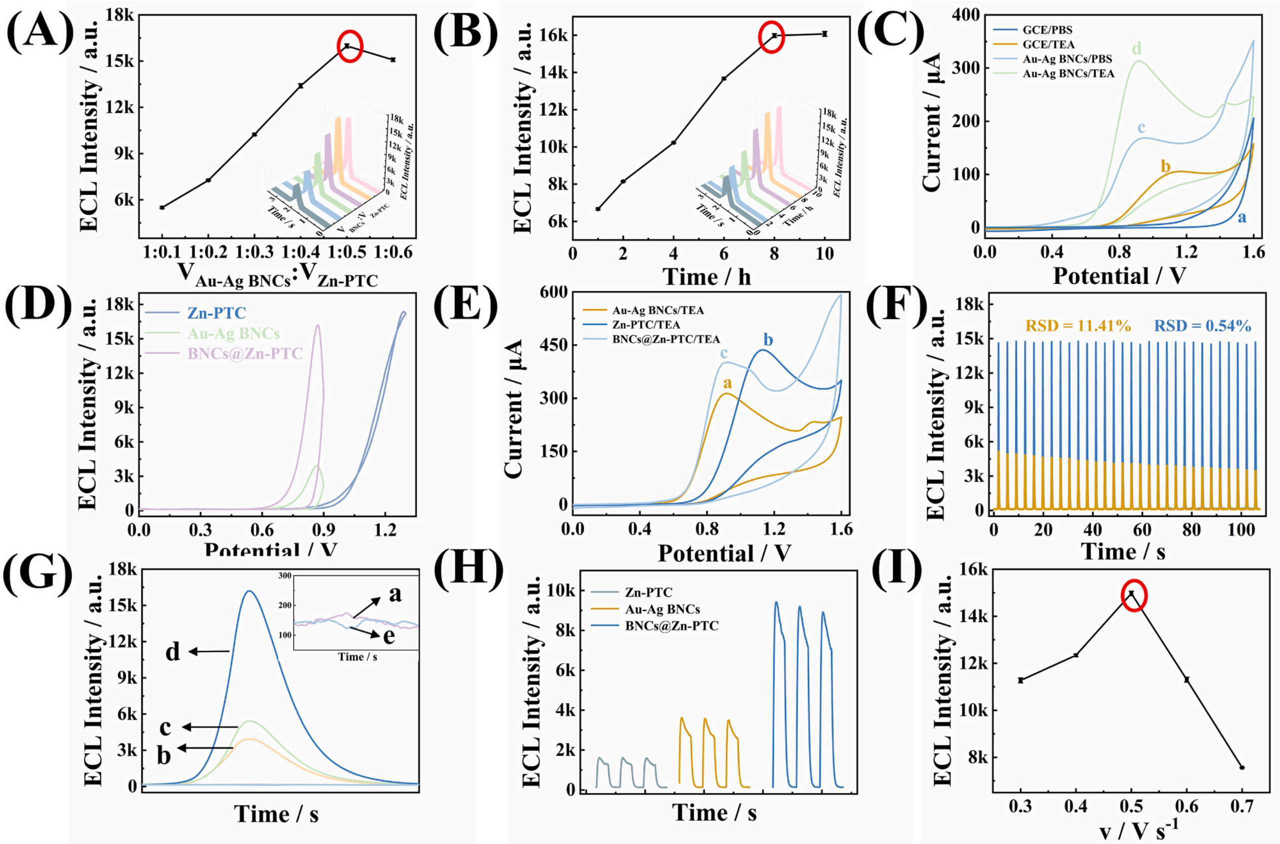

Fig. 3. Optimization of BNCs@Zn-PTC synthesis: (A) the ratio of Au-Ag BNCs: Zn-PTC and (B) reaction time. (C) CV curves of bare GCE (curve a) in 0.1 M PBS (pH = 7.4), Au-Ag BNCs/GCE in 0.1 M PBS (pH = 7.4) (curve c), bare GCE (curve b), and Au-Ag BNCs/GCE (curve d) in 0.1 M PBS (pH = 7.4) containing 20 mM TEA (a co-reactant). (D) Comparison of luminescence potentials of Zn-PTC, Au-Ag BNCs and BNCs@Zn-PTC. (E) CV curves of Au-Ag BNCs, Zn-PTC and BNCs@Zn-PTC in 0.1 M PBS (pH = 7.4) containing 20 mM TEA (a co-reactant). (F) Stability of Au-Ag BNCs (yellow line) and BNCs@Zn-PTC (blue line). (G) Comparison of ECL intensity of (a) GCE, (b) Au-Ag BNCs, (c) Zn-PTC, (d) BNCs@Zn-PTC in 20 mM TEA, and (e) BNCs@Zn-PTC in 0.1 M PBS (pH = 7.4). (H) ECL emission of Zn-PTC, Au-Ag BNCs and BNCs@Zn-PTC in 0.1 MC PBS (pH = 7.4) containing 20 mM TEA. SP parameters: $V_1 = 0.87$ V, $t_1 = 1$ s, $V_2 = 0$ V, and $t_2 = 10$ s. (I) Optimization of ECL detection scanning speed in ECL detection.

(curve c) is similar to that of Au-Ag BNCs alone, which suggests that the reaction primarily involves Au-Ag BNCs in the TEA system after the composite is formed rather than Zn-PTC. Pure Au-Ag BNCs and BNCs@Zn-PTC were tested under the same conditions, and the analysis of data from 30 cycles revealed that their relative standard deviations (RSDs) were 11.41 % and 0.54 %, respectively (Fig. 3F). This indicates that the composite material is significantly more stable.

These results demonstrate that the composite BNCs@Zn-PTC exhibits superior ECL performance compared to pure Au-Ag BNCs.

3.3. *Mechanism of the BNCs@Zn-PTC + TEA ECL reaction system*

To further investigate its ECL mechanism, the BNCs@Zn-PTC + TEA system was characterized by ECL at the potential range of 0–0.9 V. As shown in Fig. 3G, the bare electrode did not exhibit an ECL signal in the TEA solution (curve a). The ECL intensities of Au-Ag BNCs and Zn-PTC alone in TEA solution were weak (curves b and c, respectively). In contrast, the composite material BNCs@Zn-PTC exhibited a strong ECL intensity in TEA solution (curve d), which is indicative of its potential for subsequent detection applications. However, without TEA, BNCs@Zn-PTC did not exhibit a significant ECL signal (curve e), which confirms that TEA acts as the co-reactant of BNCs@Zn-PTC.

Based on these results and previous related reports, the occurrence of the in-system ECL resonance energy transfer (ECL-RET) in BNCs@Zn-PTC is as follows [34,35]. Initially, Zn-PTC is oxidized to form Zn-PTC$^{\bullet+}$. Concurrently, TEA is oxidized to produce the strongly reducing radical TEA$^{\bullet+}$, which further loses protons to form TEA$^{\bullet}$. Subsequently, TEA$^{\bullet}$ reacts with Zn-PTC$^{\bullet+}$ in a redox reaction to generate excited-state Zn-PTC* that then returns to the ground state while emitting ECL radiation.

In the ECL-RET system, Zn-PTC* acts as an energy donor that transfers energy to Au-Ag BNCs to generate excited-state Au-Ag BNCs*. These excited-state Au-Ag BNCs* then return to the ground state while producing ECL radiation. Consequently, the ECL signal of Zn-PTC decreased, whereas the ECL intensity of Au-Ag BNCs increased. The following equations illustrate the ECL enhancement mechanism of this system:

$$\mathrm{Zn-PTC} \rightarrow \mathrm{Zn-PTC}^{\cdot+} + e^{-} \tag{1}$$

$$\mathrm{TEA} \rightarrow \mathrm{TEA}^{\cdot+} + e^{-} \tag{2}$$

$$\mathrm{TEA}^{\cdot+} \rightarrow \mathrm{TEA}^{\cdot} + \mathrm{H}^{+} \tag{3}$$

$$\mathrm{Zn-PTC}^{\cdot+} + \mathrm{TEA}^{\cdot} \rightarrow \mathrm{Zn-PTC}^{*} + \mathrm{products} \tag{4}$$

$$\mathrm{Zn-PTC}^{*} \rightarrow \mathrm{Zn-PTC} + h\nu \tag{5}$$

$$\mathrm{Zn-PTC}^{*} + \mathrm{Au-Ag\ BNCs} \rightarrow \mathrm{Au-Ag\ BNCs}^{*} + \mathrm{Zn-PTC} \tag{6}$$

$$\mathrm{Au-Ag\ BNCs}^{*} \rightarrow \mathrm{Au-Ag\ BNCs} + \mathrm{hv} \tag{7}$$

These equations illustrate how the ECL enhancement mechanism in the BNCs@Zn-PTC + TEA system occurs through a series of redox and energy transfer reactions, resulting in enhanced ECL signals.

3.4. Feasibility of the ECL biosensor

The assembly process of the sensor was characterized by polypropylene gel electrophoresis. As shown in Fig. S6A, lane 1 contains single-stranded DNA 1, while lane 2 contains the Apt/DNA 1 double-stranded mixture. Lanes 3 and 4 contain single-stranded MT and DNA 3, respectively. Lane 5 shows the DNA 2/DNA 3/MT triple-stranded complex. Lane 6 shows the Apt/DNA 1 double-stranded mixture and the DNA 2/DNA 3/MT triple-stranded complex as two separated bright bands, an indication that DNA 1 does not hybridize with the triple-stranded complex in the absence of the target CA125. In lane 7, the target CA125 was added to lane 6, resulting in higher production of a separate DNA 3 strand and a single bright band lower level than the triple-stranded complex. Comparing this band with bands in the later lane, we identified that the band represented the DNA 1/DNA 2/MT triple-stranded complex. This suggests that the target CA125 binds to the Apt strand, causing the displaced DNA 1 strand to bind to the DNA 2/DNA 3/MT triple-stranded complex and the displacement of the DNA 3 strand. Lane 8 shows three bright bands and one darker band. The darker band represents the DNA 1/DNA 2/MT triple-stranded complex, while the three bright bands represent the DNA 3 strand, the MT strand, and the DNA 2/F double-stranded complex. Comparing lane 9 with lane 8 showed that the SDR reaction did not occur without the DNA 1 strand. Lane 10 displays the DNA 2/F double-stranded complex. As shown in Fig. S6B, the first three lanes contained hairpin H1, hairpin H2, and MT chain of the secondary target, respectively. Lane 4 shows separated bands corresponding to H1 and MT, as well as a band indicating that the MT chain opened hairpin H1. Lane 5 shows two bright bands that represent the binding of hairpin H1 to hairpin H2 and that the MT chain underwent cycling. Lane 6 exhibits two separated bright bands corresponding to hairpin H1 and hairpin H2, indicating that hairpin H1 cannot be hybridized with hairpin H2 without the presence of the MT chain of the secondary target.

3.5. Characterization of the assembly process of the sensor

The assembly process of the sensor was characterized by CV and electrochemical impedance spectroscopy (EIS). As shown in Fig. 4A, the bare electrode in 5.0 mM $[Fe(CN)_6]^{3-/4-}$ solution exhibited two clear redox peaks (curve a). When BNCs@Zn-PTC was modified on the electrode surface, the redox peak currents decreased (curve b). The addition of hairpin H1 on the modified electrode surface further reduced the redox peak currents (curve c), due to the repulsive force caused by the negatively charged DNA exerted on the redox process in the $[Fe(CN)_6]^{3-/4-}$ solution. After treating the electrode with HT, the redox peak current (curve d) was further reduced, which is indicative of the successful blocking of non-specific binding sites on the electrode surface. The decrease in the current (curve e) can be attributed to the presence of the modified Fc on hairpin H2, which hinders the electron transfer and exerts a repulsive force on the redox process in the solution. These results demonstrate the successful assembly of the sensor.

The EIS plots can be used to compare to the electron transfer resistance (Ret) during sensor assembly [36,37], as shown in Fig. 4B. Based on the EIS data obtained from the measurements, we constructed an equivalent circuit model and analyzed the data by ZView. The EIS data obtained from the simulation was compared with the experimental data (Fig. S11) to prove the accuracy of the equivalent circuit model and to obtain the fitted value of the electron transfer resistance. The electron transfer ability can be compared by comparing the Ret of different data. The Ret of curve a was smaller compared to that of curve b, which increased significantly after material modification. When hairpin H1 was added dropwise on the surface of the modified electrode, the Ret of curve c increased due to the resistance from surrounding DNA molecules. Both HT and Fc are non-conducting, and Fc can hinder the electron transfer, causing the Ret of curves d and e to further increase. These results confirm the successfulness of the step-by-step assembly process of the biosensor.

3.6. Analytical performance of the biosensor

The response of the sensor to different concentrations of target CA125 was examined under optimal experimental conditions. As shown in Fig. 5A, the ECL intensity gradually decreased as the CA125 concentration was increased from 1 μU mL^{-1} to 10 U mL^{-1}. Additionally, the small differences between the ECL intensity of all groups, at each concentration, indicated that the sensor possesses high stability. A linear relationship between the logarithmic values of ECL intensity and CA125 concentration was observed (Fig. 5B). The linear regression equation was $I = -1436.03\lg c + 4313.74$, and the linear correlation coefficient (R^2) was 0.9985. The detection limit of the biosensor was determined to be 0.24 μU mL^{-1} (S/N = 3). This method was demonstrated to have an excellent sensitivity and a low detection limit compared to those of other published assays (Tables S2 and S3).

3.7. Specificity, stability and reproducibility of the ECL biosensor

To evaluate the selectivity of the biosensor, three samples containing high concentrations of disease-related interfering proteins—carcinoembryonic antigen (CEA), immunoglobulin (IgG), and MUC1 protein (MUC1)—as well as their mixtures were selected. As shown in Fig. 5C, the incubation with 10 ng mL^{-1} CEA, IgG, and MUC1 resulted in an ECL intensity similar to the intensity of the blank sample. However, when incubating with 1 U mL^{-1} CA125 or a mixture of CA125 and interfering substances, the ECL intensity significantly decreased, which is an indication that the biosensor has good specificity and selectivity for CA125.

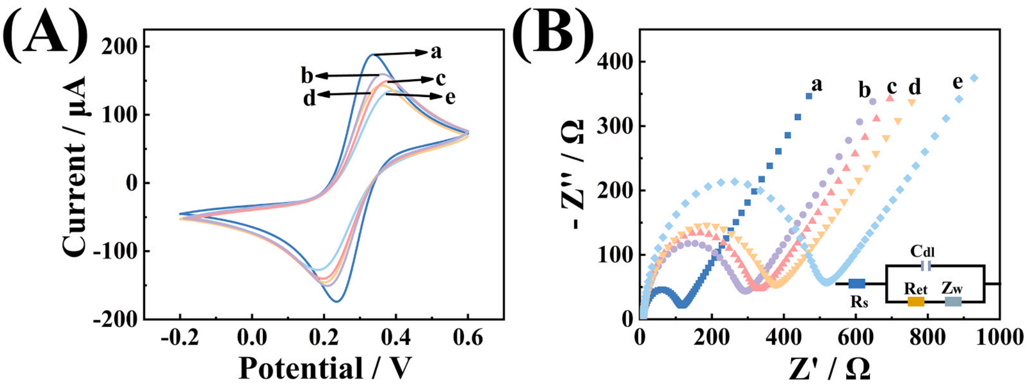

Fig. 4. (A) CV and (B) EIS curves measured during the stepwise modification process. a−e: GCE, GCE/BNCs@Zn-PTC, GCE/BNCs@Zn-PTC/H1, GCE/BNCs@Zn-PTC/H1/HT and GCE/BNCs@Zn-PTC/H1/HT/H2.

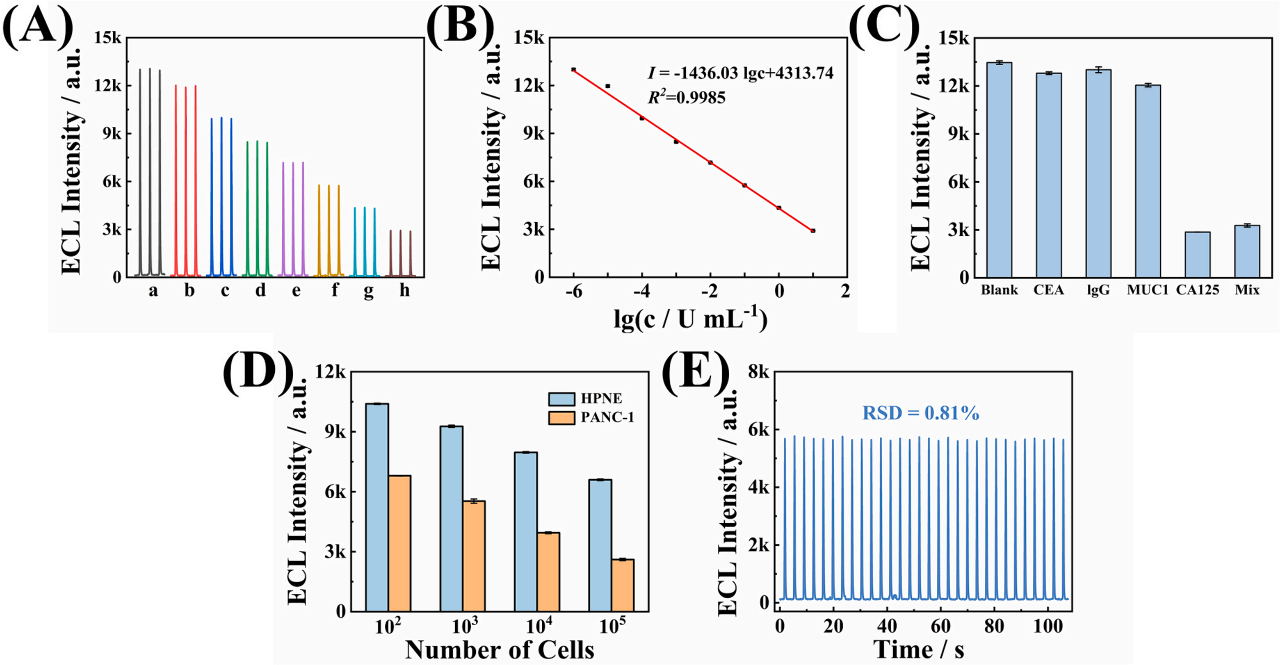

Fig. 5. (A) ECL response of the biosensor to CA125 at different concentrations. (B) Linear correlation between intensity (I) and log c (CA125 concentration). (C) Specificity of the ECL biosensor. (D) Detection of CA125 in hTERT-HPNE and PANC-1 cells by the ECL biosensor. (E) Stability of BNCs@Zn-PTC (blue line) and the ECL biosensor (yellow line).

The reproducibility of the ECL responses was further investigated by comparing different electrodes from the same batch, as well as the same electrode across different batches (Fig. S9). The ECL intensities of different electrodes and at different times were not significantly different, with relative standard deviations (RSD) of 0.99 % and 0.51 %, respectively. This demonstrates that the constructed sensors have good reproducibility. Furthermore, as shown in Fig. 5E, the ECL intensity of the constructed sensor was not significantly changed (RSD = 0.81 %) after being scanned continuously for 30 cycles when the target concentration was 0.1 U mL^{-1}. This indicates that the sensor has excellent stability.

3.8. Application of the ECL biosensor in real samples

To evaluate the applicability of the prepared biosensors, CA125 was detected in hTERT-HPNE cells (human normal pancreatic cells) and PANC-1 cells (pancreatic cancer cells), and recovery experiments were performed using serum samples diluted by the standard addition method. The expression of CA125 in hTERT-HPNE cells and PANC-1 cells was investigated by using these two cell lysates as reaction fluids. As shown in Fig. 5D, the ECL intensity gradually decreased with increasing number of cell, and the difference between the ECL intensities of the two cell types became more pronounced. This indicates that CA125 is highly expressed in PANC-1 cells, which is consistent with previously reported results. The recovery experiments were performed by adding different concentrations of the test substance to human serum after a 50-fold dilution, and then comparing the measured results to the linear results. Results from the spiked recovery experiment are presented in Table 1. The results showed that the recoveries ranged from 100.28 % to 107.24 % with RSDs ranging from 0.14 % to 0.84 %. These results demonstrate that the constructed ECL biosensor is suitable for practical applications and shows good analytical performance in the detection of pancreatic cancer. The sensor holds broad clinical application prospects.

Table 1
Recovery of target spiked in human serum samples (n = 3).

Target	Added	Found	RSD	Recovery
CA125	1.00 U mL^{-1}	1002.79 mU mL^{-1}	0.14 %	100.28 %
	1.00 mU mL^{-1}	1.03 mU mL^{-1}	0.75 %	101.96 %
	1.00 μU mL^{-1}	1.07 μU mL^{-1}	0.84 %	107.24 %

4. Conclusion

In the exploration of novel ECL luminescence at the anode, we constructed a composite material with excellent electrochemical luminescence performance. The framework structure of Zn-PTC could effectively reduce the ACQ effect of PTCA and enhance electron transfer efficiency, thus further improving the ECL intensity of the luminescence. Au-Ag BNCs synthesized using Met as a capping and stabilizing agent can allow for the generation of low-potential ECL at the anode; however, they suffer from low stability and low efficiency. By using Zn-PTC as the donor in the ECL-RET system and Au-Ag BNCs as the acceptor, we synthesized composites with the combined advantages of the two components and were able to generate low-potential ECL at the anode. Subsequently, an ECL biosensor for the detection of CA125 was constructed using SDR-CHA double amplification. The sensor was demonstrated to have a low detection limit, a wide detection range, and the ability to determine the resectability of pancreatic cancer in patients. These findings demonstrate the potential of the constructed ECL biosensor in practical applications such as clinical diagnostics, particularly in the detection and management of pancreatic cancer.

CRediT authorship contribution statement

Daqian Song: Supervision, Resources, Project administration. **Ziwei Zhang:** Writing – review & editing, Visualization, Resources. **Pinyi Ma:** Writing – review & editing, Project administration, Funding acquisition, Data curation, Conceptualization. **Jukun Yang:** Investigation, Data curation. **Yongli Wu:** Methodology, Investigation. **Mo Ma:** Investigation, Formal analysis. **Zhuoxin Ye:** Investigation, Data curation. **Yuxuan Chen:** Writing – original draft, Investigation, Formal analysis, Data curation, Conceptualization.

Declaration of Competing Interest

The authors declare that they have no known competing financial interests or personal relationships that could have appeared to influence the work reported in this paper.

Acknowledgments

This work was supported by the Science and Technology Developing Foundation of Jilin Province of China (20230101033JC), and the National Natural Science Foundation of China (22074052 and 22004046).

Appendix A. Supporting information

Supplementary data associated with this article can be found in the online version at doi:10.1016/j.snb.2024.137136.

Data availability

Data will be made available on request.

References

[1] J. Zhang, F. Teng, B. Hu, W. Liu, Y. Huang, J. Wu, Early diagnosis and prognosis prediction of pancreatic cancer using engineered hybrid core-shells in laser desorption/ionization mass spectrometry, Adv. Mater. 36 (2024) 2311431.

[2] Q. Wang, B. Šabanović, A. Awada, C. Reina, A. Aicher, J. Tang, Single-cell omics: a new perspective for early detection of pancreatic cancer? Eur. J. Cancer 190 (2023) 112940.

[3] P. Cheng, S. Ming, W. Cao, J. Wu, Q. Tian, J. Zhu, Recent advances in sonodynamic therapy strategies for pancreatic cancer, WIREs Nanomed. Nanobiotechnol. 16 (2024) e1945.

[4] D.P. O'Brien, N.S. Sandanayake, C. Jenkinson, A. Gentry-Maharaj, S. Apostolidou, E.-O. Fourkala, Serum CA19-9 is significantly upregulated up to 2 years before diagnosis with pancreatic cancer: implications for early disease detection, Clin. Cancer Res. 21 (2015) 622–631.

[5] S. Guo, A. Fesler, H. Wang, J. Ju, microRNA based prognostic biomarkers in pancreatic cancer, Biomark. Res. 6 (2018) 1–5.

[6] R. Yamada, J. Tsuboi, Y. Murashima, T. Tanaka, K. Nose, H. Nakagawa, Advances in the early diagnosis of pancreatic ductal adenocarcinoma and premalignant pancreatic lesions, Biomedicines 11 (2023) 1687.

[7] M. Grunnet, I.J. Christensen, U. Lassen, L.H. Jensen, M. Lydolph, J.J. Knox, Decline in CA19-9 during chemotherapy predicts survival in four independent cohorts of patients with inoperable bile duct cancer, Eur. J. Cancer 51 (2015) 1381–1388.

[8] J.F. Liu, K.N. Moore, M.J. Birrer, S. Berlin, U.A. Matulonis, J.R. Infante, Phase I study of safety and pharmacokinetics of the anti-MUC16 antibody–drug conjugate DMUC5754A in patients with platinum-resistant ovarian cancer or unresectable pancreatic cancer, Ann. Oncol. 27 (2016) 2124–2130.

[9] H.M.H. Diab, H.G. Smith, K.K. Jensen, L.N. Jørgensen, The current role of blood-based biomarkers in surgical decision-making in patients with localised pancreatic cancer: a systematic review, Eur. J. Cancer 154 (2021) 73–81.

[10] H. Li, Q. Yang, Z. Wang, F. Li, Iridium complex with specific intercalation in the G-quadruplex: a phosphorescence and electrochemiluminescence dual-mode homogeneous biosensor for enzyme-free and label-free detection of MicroRNA, ACS Sens 8 (2023) 1529–1535.

[11] X. Wang, H. Chen, M. Sun, B. Chen, H. Xu, Y. Fan, ECL and visual dual-mode detection of miRNA-21 based on HRP/Au NPs composite probe and CRISPR/Cas12a strategy, Sens. Actuators B-Chem. 425 (2025).

[12] R. Wu, Y. Cao, Y. Liu, Y. Zhou, Z. Chen, J.-J. Zhu, Alkynyl ligands templated assemblies of silver nanoclusters with exceptional electrochemiluminescence activity for pancreatic cancer specific tsRNAs measurement, Anal. Chem. (2024).

[13] J. Fang, L. Dai, R. Feng, W. Cao, X. Ren, X. Li, Strong aggregation-induced electrochemiluminescence of pyrene-coordination metal-organic frameworks coupled with zero-valent iron as novel accelerator for ultrasensitive immunoassay, J. Colloid Interface Sci. 665 (2024) 934–943.

[14] X. Zhang, P. Wang, Y. Nie, Q. Ma, Recent development of organic nanoemitter-based ECL sensing application, TrAC-Trend Anal. Chem. 143 (2021) 116410.

[15] X. Song, L. Zhao, X. Ren, T. Feng, H. Ma, D. Wu, Highly efficient PTCA/Co_3O_4/CuO/$S_2O_8^{2-}$ ternary electrochemiluminescence system combined with a portable chip for bioanalysis, ACS Sens 7 (2022) 2273–2280.

[16] J. Fang, L. Dai, R. Feng, D. Wu, X. Ren, W. Cao, High-performance electrochemiluminescence of a coordination-driven J-aggregate K-PTC MOF regulated by metal–phenolic nanoparticles for biomarker analysis, Anal. Chem. 95 (2022) 1287–1293.

[17] S. Xiang, J. Li, M. Shi, H. Yang, R. Cai, W. Tan, A novel ECL aptasensor for ultra-highly sensitive detection of patulin based on terbium organic gels as Co-reaction accelerator in a 3, 4, 9, 10-perylenetetracarboxylic acid/$K_2S_2O_8$ system, Sens. Actuators B-Chem. 394 (2023) 134365.

[18] L.-l Xu, W. Zhang, L. Shang, R.-n Ma, L.-p Jia, W.-l Jia, Perylenetetracarboxylic acid and carbon quantum dots assembled synergistic electrochemiluminescence nanomaterial for ultra-sensitive carcinoembryonic antigen detection, Biosens. Bioelectron. 103 (2018) 6–11.

[19] J. Zhao, W.-B. Liang, Y.-M. Lei, Y.-X. Ou, Y.-Q. Chai, R. Yuan, An efficient electrochemiluminescence amplification strategy via bis-co-reaction accelerator for sensitive detection of laminin to monitor overnutrition associated liver damage, Biosens. Bioelectron. 98 (2017) 317–324.

[20] J. Li, M. Xi, L. Hu, H. Sun, C. Zhu, W. Gu, A controlled release aptasensor utilizing AIE-active MOFs as high-efficiency ECL nanoprobe for the sensitive detection of adenosine triphosphate, Anal. Chem. 96 (2024) 2100–2106.

[21] X. Qin, Z. Zhan, Z. Ding, Progress in electrochemiluminescence biosensors based on organic framework emitters, Curr. Opin. Electrochem. 39 (2023) 101283.

[22] Y. Liu, X. Zhao, C. Fang, Z. Ye, Y.-B. He, D. Lei, Activating aromatic rings as Na-ion storage sites to achieve high capacity, Chem 4 (2018) 2463–2478.

[23] Z. Wang, R. Ding, X. Li, J. Zhang, L. Yang, Y. Wang, Blocking accretion enables dimension reduction of metal-organic framework for photocatalytic performance, Small 19 (2023) 2305308.

[24] J.-M. Wang, L.-Y. Yao, W. Huang, Y. Yang, W.-B. Liang, R. Yuan, Overcoming aggregation-induced quenching by metal−organic framework for electrochemiluminescence (ECL) enhancement: Zn-PTC as a new ECL emitter for ultrasensitive MicroRNAs detection, ACS Appl. Mater. Interfaces 13 (2021) 44079–44085.

[25] Y. Li, G. Zhao, B. An, K. Xu, D. Wu, X. Ren, Multimetal-based metal–organic framework system for the sensitive detection of heart-type fatty acid binding protein in electrochemiluminescence immunoassay, Anal. Chem. 96 (2024) 4067–4075.

[26] W. Zhong, Y. Zhang, H. Zhao, Z. Liang, J. Shi, Q. Ma, High electrochemical active Au-NP/2D zinc-metal organic frameworks heterostructure-based ECL sensor for the miRNA-522 detection in triple negative breast cancer, Talanta 265 (2023) 124875.

[27] H.-H. Deng, L.-N. Zhang, S.-B. He, A.-L. Liu, G.-W. Li, X.-H. Lin, Methionine-directed fabrication of gold nanoclusters with yellow fluorescent emission for Cu^{2+} sensing, Biosens. Bioelectron. 65 (2015) 397–403.

[28] Q. Huang, X. Zhu, X. Sun, X. Wang, Y. Li, H. Ma, Synergetic-effect-enhanced electrochemiluminescence of zein-protected Au–Ag bimetallic nanoclusters for CA15-3 detection, Anal. Chim. Acta 1278 (2023) 341760.

[29] L. Fu, X. Gao, S. Dong, H.-Y. Hsu, G. Zou, Surface-defect-induced and synergetic-effect-enhanced NIR-II electrochemiluminescence of Au–Ag bimetallic nanoclusters and its spectral sensing, Anal. Chem. 93 (2021) 4909–4915.

[30] H. Li, M. Shao, J. Fang, Y. Li, X. Sun, X. Ren, Metal-Organic framework incorporated luminescent PTCA combined with novel co-reactant accelerator for ultra-sensitive electrochemiluminescence detection of CA19-9, Chem. Eng. J. 495 (2024).

[31] X. Song, L. Zhao, N. Zhang, L. Liu, X. Ren, H. Ma, Zinc-based metal–organic framework with MLCT properties as an efficient electrochemiluminescence probe for trace detection of trenbolone, Anal. Chem. 94 (2022) 14054–14060.

[32] J. Zhao, Y.-M. Lei, Y.-Q. Chai, R. Yuan, Y. Zhuo, Novel electrochemiluminescence of perylene derivative and its application to mercury ion detection based on a dual amplification strategy, Biosens. Bioelectron. 86 (2016) 720–727.

[33] B. Zhang, Y. Wang, Y. Wang, F. Huo, P.G. Karmaker, L. Chen, Chameleon-like response mechanism of gold–silver bimetallic nanoclusters stimulated by sulfur ions and their application in visual fluorescence sensing, Anal. Chem. 96 (2024) 5029–5036.

[34] X. Zhou, M. Li, S. Niu, J. Han, S. Chen, G. Xie, Copper nanocluster-$Ru(dcbpy)_3^{2+}$ as a cathodic ECL-RET probe combined with 3D bipedal DNA walker amplification for bioanalysis, Analyst 148 (2023) 114–119.

[35] L. Guo, Y. Zhou, Q. Feng, H. Yin, DNA tetrahedral nanostructure-corbelled DNA walker for intramolecular electrochemiluminescence resonance energy transfer sensing of tumor exosomes, Sens. Actuators B-Chem. 410 (2024) 135735.

[36] M. Jiang, M. Wang, W. Lai, C. Zhao, C. Hong, X. Qiao, Construction of an aptamer sensor for sensitive detection of AOH based on the enhancement of light/electric dual signaling response of Ru/Cu-THQ by Ag NCs, Chem. Eng. J. 485 (2024) 149911.

[37] X. Zhang, Z. Li, X. Wang, L. Hong, X. Yin, Y. Zhang, CRISPR/Cas12a integrated electrochemiluminescence biosensor for pufferfish authenticity detection based on $NiCo_2O_4$ NCs@Au as a coreaction accelerator, Food Chem. 445 (2024) 138781.

Yuxuan Chen is currently a master degree student in College of Chemistry, Jilin University. Her interest is electrochemical biosensor.

Zhuoxin Ye is currently a PhD student in College of Chemistry, Jilin University. Her interest is electrochemical biosensor.

Mo Ma is currently a PhD student in School of Pharmacy, Jilin University. His interest is spectral analysis.

Yongli Wu is currently a PhD student in College of Chemistry, Jilin University. Her interest is electrochemical biosensor.

Jukun Yang is currently a PhD student in College of Chemistry, Jilin University. Her interest is spectral analysis.

Pinyi Ma received his doctor's degree from College of Chemistry, Jilin University in 2017 and he is an associate professor in that school. His research area is spectral analysis.

Ziwei Zhang received her PhD degree in biophysics in Cornell University in 2010. She is currently an associate professor in Jilin University. Her research interest focuses on spectral analysis and electron spin resonance spectroscopy.

Daqian Song received his doctor's degree from College of Chemistry, Jilin University in 2003 and he is a professor in that school. His research areas are spectral and chromatography analysis.